Chronic alcohol induces subcircuit-specific striatonigral plasticity enhancing the sensorimotor basal ganglia role in action execution

Giacomo Sitzia[1,2], Sebastiano Bariselli[1,3], Alexa Gracias[1], David M. Lovinger*[1]

[1]Laboratory for Integrative Neuroscience, National Institute on Alcohol Abuse and Alcoholism, National Institutes of Health, Rockville, MD, USA

[2]Department of Neuroscience, Faculty of Health and Medical Sciences, University of Copenhagen, Copenhagen, Denmark

[3]IRCCS Humanitas Research Hospital, Via Manzoni 56, 20089 Rozzano, Milan, Italy

***Corresponding author:** David M. Lovinger, lovindav@mail.nih.gov

Abstract

Functional deficits in basal ganglia (BG) circuits contribute to cognitive and motor dysfunctions in Alcohol Use Disorder. Chronic alcohol exposure alters synaptic function and neuronal excitability in the dorsal striatum, but it remains unclear how it affects BG output that is mediated by the substantia nigra pars reticulata (SNr). Here we describe a neuronal subpopulation-specific synaptic organization of striatal and subthalamic (STN) inputs to the medial and lateral SNr. Chronic alcohol exposure (CIE) potentiated dorsolateral striatum (DLS) inputs but did not change dorsomedial striatum (DMS) and STN inputs to the SNr. Chemogenetic inhibition of DLS direct pathway neurons revealed an enhanced role for DLS direct pathway neurons in execution of an instrumental lever-pressing task. Overall, we reveal a subregion-specific organization of striatal and subthalamic inputs onto the medial and lateral SNr and find that potentiated DLS-SNr inputs are accompanied by altered BG control of action execution following chronic alcohol exposure.

Introduction

Alcohol is one of the most abused drugs worldwide. Alcohol Use Disorder (AUD) is a disease characterized by loss of control over alcohol intake[1,2], with devastating consequences for the affected people and society. Alcohol can affect brain function through acute, direct interactions with multiple substrates including, but not limited to, neurotransmitter receptors[3,4]. Alcohol also produces long-term changes in neural circuits[3,5] which contribute to long term cognitive and motor dysfunctions. Therefore, disentangling the complexity of brain circuits and their susceptibility to alcohol effects is necessary to refine therapeutic strategies targeting behavioral dysfunctions in AUD.

Brain regions of the basal ganglia (BG) coordinate motor and non-motor behaviors based on the present context and past experiences[6–9], and their dysfunction has been implicated in the development of pathological habits and altered control of goal-directed behavior in AUD[10]. BG circuits control diverse functional outputs through the GABAergic projection neurons of the substantia nigra pars reticulata (SNr) and the globus pallidus internal segment (GPi), which target brainstem, midbrain and thalamic nuclei[11–13]. The BG control the SNr via striatal GABAergic direct pathway inputs and subthalamic nucleus (STN) glutamatergic indirect pathway inputs, that according to the classical view are thought to promote or suppress behavioral outputs influenced by the SNr, respectively[8,9,14]. The main neuronal population of the dorsal striatum (DS) are the spiny projection neurons (SPNs), divided into direct pathway SPNs (dSPNs) targeting the SNr/GPi and indirect pathway SPNs (iSPNs) targeting the globus pallidus external segment (GPe). The GPe in turn projects to the STN and the SNr. The direct and indirect pathway are a circuit backbone shared across anatomically parallel BG circuits with distinct functional roles[15–17]. The dorsomedial (DMS) and dorsolateral (DLS) subregions of the striatum receive associative and sensorimotor cortical inputs[18,19] and have been implicated in goal-directed (DMS) and habitual (DLS) action control[6]. Striatal projections to the SNr are topographically organized, hence spatially distinct subpopulations in the medial (^{M}SNr) and ventrolateral (^{L}SNr) SNr receive inputs from the DMS and DLS[12,20]. Understanding how alcohol affects BG circuits requires a refined knowledge of the organization of synaptic inputs to subpopulations of SNr neurons.

The intrinsic physiological properties of SNr neurons vary along the mediolateral axis of the nucleus[13]. Molecularly identified subpopulations of SNr neurons include a majority of parvalbumin (PV^+) expressing neurons, enriched in the ventrolateral aspects of the nucleus, as well as other subpopulations that have been characterized based on the expression of the vesicular GABA transporter (VGAT), calretinin (CR) and Glutamate Decarboxylase 2 enzyme (GAD2)[13,21–23]. The physiological properties and projection patterns of PV^+ SNr neurons differentiates them from other SNr neuron subpopulations[21,24]. The molecular and functional heterogeneity of SNr neurons is also tuned to the diversity of neuronal targets innervated by the SNr[13]. However, whether synaptic inputs to distinct SNr neuron subpopulations are organized to reflect their functional heterogeneity remains unclear.

The synaptic effects of acute and chronic alcohol exposure on the BG have been investigated in animal studies mainly focused on striatal circuits[25,26]. These experiments showed that acute alcohol effects and maladaptive circuit adaptations following chronic alcohol exposure vary according to the striatal cell type, synaptic input, and subregion examined. In a series of seminal studies, Corbit & Janak demonstrated that the control of alcohol self-administration in rats shifts from goal-directed to habitual upon repeated (>2 weeks) exposure due to an increased engagement of the DLS over the DMS[27,28]. Within the DLS, acute exposure of striatal slices to alcohol decreases GABAergic tone on SPNs, inhibits SPN-SPN synapses and fast spiking interneuron-SPN synapses[29]. This suggests that acute alcohol exposure initiates a disinhibition of DLS circuits. Within the DMS, altered synaptic plasticity of the medial prefrontal cortex (mPFC)-DMS inputs contributes to perseveration in alcohol-seeking behaviors[30,31], whereas weakened orbitofrontal cortex (OFC)-DMS inputs impairs goal-directed action control following chronic alcohol exposure[32,33]. These studies indicate that chronic alcohol exposure induces synaptic maladaptations in specific striatal subcircuits to cause

distinct behavioral alterations. However, the susceptibility to alcohol effects of BG output structures downstream of the striatum remains poorly understood. This limits our understanding of the behavioral and circuit adaptations induced by chronic alcohol exposure.

Here, we asked whether synaptic plasticity in SNr contributes to altered action execution following chronic alcohol exposure in mice. First, we used optogenetics-assisted circuit mapping and found that DMS-SNr and DLS-SNr inputs differ in their presynaptic properties and target distinct SNr subpopulations. Moreover, we found that indirect pathway inputs from the STN are biased to the lateral SNr. We then demonstrated that chronic alcohol exposure potentiates DLS-SNr inputs without changing the strength and presynaptic properties of STN-SNr and DMS-SNr inputs. Finally, we found that chemogenetic inhibition of DLS-SNr inputs impaired action execution in mice exposed to chronic alcohol but not in control mice. Overall, we identified a synaptic basis for an abnormal functional control of action execution in the sensorimotor BG circuit following chronic alcohol exposure.

Results

1. Input-output organization of the DMS-SNr and DLS-SNr subcircuits

Our first goal was to establish the functional relationships between distinct striatal inputs and their targets in the SNr. We virally expressed the opsin Chronos in the DMS or DLS using injections of an adeno-associated virus (AAV) (pAAV5-Syn-Chronos-GFP) and performed *ex vivo* whole-cell patch-clamp recordings coupled with local field optogenetic stimulation in SNr slices (Fig. 1A). As expected, DMS- GFP$^+$ terminals were detected in the medial portion of the SNr (^{M}SNr). In contrast, DLS- GFP$^+$ terminals were detected in the ventrolateral portion of the SNr (^{L}SNr)[12,16,20] (Fig. 1A). Therefore, we focused our recordings on the ^{M}SNr to characterize DMS- SNr synapses and on the ^{L}SNr to characterize DLS- SNr synapses. The amplitude of oIPSCs at DMS-^{M}SNr (2.5 ± 0.6 nA) and DLS-^{L}SNr (1.6 ± 0.4 nA) synapses was not statistically different (Fig. supp. 1A), while the oIPSC latency to peak was statistically different but consistent in both synapses with monosynaptic inputs (DMS-^{M}SNr 3.8 ± 0.1 ms; DLS-^{L}SNr 5.1 ± 0.2 ms) (Fig. supp. 1B). We compared the presynaptic properties of DMS-^{M}SNr and DLS-^{L}SNr synapses by calculating the paired-pulse ratio (PPR) using stimuli delivered with a 50 ms interpulse interval. We found that PPRs at DMS-SNr synapses were characterized by short-term depression (PPR: 0.87 ± 0.06) and PPRs at DLS-SNr synapses were characterized by short-term facilitation (PPR: 1.29 ± 0.12), and that overall PPRs were significantly different between the two synapses (Fig. 1B). This difference was further evidenced during a train of 10 stimuli delivered at 20 Hz (Fig. supp. 1C). These results indicate that DMS-^{M}SNr and DLS-^{L}SNr synapses differ in their presynaptic properties.

In a subset of these experiments, we used PVCre-TdTom mice to label parvalbumin-expressing (PV$^+$) SNr neurons, previously indicated as the major GABAergic subpopulation of the SNr[13,34]. We found a significantly higher proportion of TdTom$^-$ neurons (PV$^-$) among DMS- connected neurons (1 TdTom$^+$, 10 TdTom$^-$) compared to a majority of TdTom$^+$ neurons (PV$^+$) among DLS- connected neurons (8 TdTom$^+$, 2 TdTom$^-$) (Fig. 1C). This first series of experiments indicated that the DMS and DLS target molecularly distinct subpopulations of SNr neurons. Next, we investigated how the firing activity of ^{M}SNr and ^{L}SNr neurons is controlled by their striatal inputs.

We used the same Chronos-assisted DMS- ^{M}SNr and DLS- ^{L}SNr circuit mapping strategy to perform current-clamp experiments identifying SNr neurons as DMS- or DLS-targeted based on the presence of an IPSP (Fig. 1D). We found that the spontaneous firing rate of DLS-targeted neurons (24.25 ± 2.5 Hz; 5/26 cells not spontaneously active) was significantly higher compared to DMS- targeted SNr neurons (17.66 ± 1. 35 Hz; 3/24 cells not spontaneously active) (Fig. 1E). The R_{in} of DMS- targeted SNr neurons (469.9 ± 40.9 MΩ) was significantly higher than DLS-targeted neurons (278.6 ± 25.4 MΩ) (Fig. 1F), which might indicate higher excitability of DMS-targeted neurons. We found fast rebound firing responses to hyperpolarization in most DMS-targeted and DLS-targeted neurons (Fig. 1G; fig. supp. F). However, a significantly higher number of DMS-targeted neurons displayed prolonged rebound firing responses when compared to DLS-targeted neurons (Fig. 1G; fig. supp. 1F). These results indicate that DMS-targeted and DLS-targeted SNr neurons differ in their intrinsic properties and post-inhibitory rebound responses.

We next studied the firing responses of SNr neurons during DMS or DLS terminal stimulation using trains of stimuli delivered at 10 and 20 Hz. We found that 10 Hz stimulation induced partial inhibition of firing at DMS- ^{M}SNr (Light off: 11.2 ± 1.8 Hz; Light on 6.7 ± 1.5 Hz) and DLS- ^{L}SNr inputs (Light off: 19.8 ± 2.7 Hz; Light on 10 ± 2.5 Hz), whereas a 20 Hz stimulation strongly inhibited firing in both the DMS-^{M}SNr input (Light off: 10.6 ± 1.1 Hz; Light on: 0.9 ± 0.6 Hz) and the DLS-^{L}SNr input (Light off: 15.2 ± 1.8 Hz; Light on 0.75 ± 0.72 Hz) (Fig. 1H). Post-inhibitory prolonged rebound responses emerged in most DMS-targeted and a subset of DLS- targeted SNr neurons in response to 10 or 20 Hz stimulation (Fig. 1I). These findings demonstrate that striatal inputs can induce post-inhibitory rebound firing in SNr neurons in a subpopulation-dependent manner.

2. Differential organization of STN inputs to the medial and lateral SNr

Due to the functional differences of direct pathway striatal inputs on distinct subregions of the SNr, we next sought to determine whether functional differences exist in indirect pathway STN inputs to the ^{M}SNr and ^{L}SNr. We virally expressed a Cre-dependent Chronos (AAV5-hSyn-FLEX-Chronos-GFP) in the STN of VGlut2-Cre mice (Fig. 2A). Here, we could not define ^{M}SNr and ^{L}SNr neurons based on their striatal input, but we based our classification on their spatial location. To ensure that we were recording from distinct SNr populations, we first confirmed that R_{in} was significantly higher in ^{M}SNr than ^{L}SNr neurons (Fig. supp. 2A), which matched previous data based on striatal input specificity (Fig. 1A). The amplitude of oEPSCs was significantly higher at STN-^{L}SNr (0.52 ± 0.1 nA) over STN-^{M}SNr (0.23 ± 0.05 nA) synapses (Fig. 2B), indicating that STN inputs are biased to the lateral SNr. We then reasoned that STN inputs might be scaled to the different intrinsic properties of SNr subpopulations. We found a significant correlation (r^2 = 0.5338) between the amplitude of oEPSCs at STN-SNr synapses and the R_{in} of recorded neurons (Fig. 2C). Using paired stimuli delivered with a 50 ms interpulse interval, we found that the PPR at STN-^{M}SNr synapses was facilitating (PPR: 1.3 ± 0.11) whereas no net facilitation or depression emerged at STN-^{L}SNr (PPR: 1.04 ± 0.04) inputs, and that PPRs at STN-^{M}SNr and STN-^{L}SNr synapses were significantly different (Fig. 2D). Hence, STN-SNr inputs are biased to the ^{L}SNr also due to higher release probability at STN-^{L}SNr synapses.

We next studied SNr firing responses while stimulating STN inputs using 20 Hz stimulus trains. The increase in firing relative to baseline produced by STN terminal stimulation was similar in ^{M}SNr (Light off: 7.5 ± 3 Hz; Light on: 39.5 ± 5 Hz) neurons compared to ^{L}SNr (Light off: 9.2 ± 2.5 Hz; Light on: 33 ± 3.7 Hz) neurons (Fig. 3H). Hence, STN inputs have different synaptic strengths in the different SNr subregions but are sufficient to induce firing in ^{M}SNr and ^{L}SNr neurons.

3. Altered DLS-SNr inputs but not DMS-SNr inputs following chronic alcohol exposure

In our circuit characterization we established key synaptic differences in DMS, DLS and STN inputs to the ^{M}SNr and ^{L}SNr, serving as a starting point to examine alcohol effects on distinct SNr subcircuits.

We virally expressed Chronos in the DMS or DLS and subjected 3–4-month-old C57BL mice to chronic intermittent alcohol vapor exposure (CIE) and a control group to air exposure (AIR) (Fig. 3A). We performed electrophysiological experiments during extended withdrawal (3-21 days post-withdrawal), a period associated with altered action control and cortico-striatal synaptic dysfunctions[25,26] following CIE. We first investigated the presynaptic properties of DMS-SNr and DLS-SNr synapses between AIR and CIE mice. We found that CIE did not induce a change in PPR at DMS- SNr synapses, whereas CIE induced an increase in PPR at DLS- SNr synapses (Fig. 3B). The increased PPR at DLS-SNr synapses might be indicative of a reduced release probability. To investigate whether the PPR changes at DLS-SNr synapses were associated with overall changes in synaptic strength, we recorded asynchronous IPSCs (aIPSCs) (Fig. 3C). We found that CIE did not alter the frequency and amplitude of aIPSCs at DMS-SNr synapses (Fig. 3D, E). Conversely, we found that CIE induced an increase in the amplitude and frequency of aIPSCs at DLS-SNr synapses (Fig. 3D, E). The increased synaptic strength at DLS-SNr synapses likely reflects a post-synaptic mechanism accompanied by a compensatory presynaptic decrease in release probability. Overall, the net effect of CIE appears to be selective potentiation of DLS-SNr synapses.

4. STN inputs to the SNr are unaltered following chronic alcohol exposure

A potentiated DLS-SNr synapse might enhance the direct pathway influence over lateral SNr output following CIE. STN inputs to the SNr, particularly those to the lateral SNr, may counteract striatal inputs to reduce SNr- mediated behavioral outputs[35]. We therefore sought to investigate whether CIE produced changes in STN inputs to the SNr. VGluT2- Cre mice were injected with a Cre- dependent version of Chronos in the STN and allocated to AIR or CIE groups. Patch- clamp recordings were performed during prolonged withdrawal (3-21 days post-withdrawal) (Fig. 4A). We found that CIE did not affect the oEPSC amplitude at STN-^{M}SNr and STN- ^{L}SNr synapses (Fig. 4B). Similarly, we found that CIE did not affect the PPR at STN- ^{M}SNr and STN- ^{L}SNr synapses (Fig. 4C). These results indicate that CIE did not alter STN inputs to the ^{M}SNr and ^{L}SNr. In summary, our synaptic characterization indicates that CIE might facilitate direct pathway control over lateral SNr output via strengthened DLS-SNr inputs.

5. Chronic alcohol exposure shifts action control to direct pathway SPNs in the DLS

Cognitive/ executive and motor impairments in AUD may be protracted during extended withdrawal. To probe whether altered DLS- SNr synapses contribute to altered cognitive/ executive and motor functions following CIE we trained mice in a random ratio instrumental procedure while performing targeted chemogenetic silencing of DLS dSPNs. Drd1-Cre+ mice or Cre- littermates were injected with AAV-DIO-hM4D(Gi)-mCherry in the DLS and randomly allocated to AIR or CIE groups (Fig. 4A). The activation of hM4D(Gi) by CNO decreased GABA release at striatonigral inputs (Fig. supp. 3C), in agreement with what previously observed in vivo at dSPN-GPe bridge collateral terminals[36]. 6-7 days after withdrawal, AIR (Cre-,

Cre+) and CIE (Cre-, Cre+) mice underwent operant conditioning for 20% sucrose reward that began with 5 days of fixed ratio 1 training and then progressed to 2 days of random ratio 10 and 4 days of random ratio 20 training (Fig. 4B). Mice received CNO (5 mg/kg) injections during random ratio (RR) training to inhibit dSPNs in the DLS. 3-way ANOVA analysis (factors: time, treatment, and genotype) revealed a significant interaction between session, genotype, and treatment in the lever press number (Fig. supp. 3A), whereas this interaction was trending for the lever press frequency (Fig. supp. 3B). This analysis revealed that chemogenetic inhibition differentially affects AIR and CIE mice depending on the session. Importantly, the lack of a main effect of alcohol indicated that alcohol exposure per se was not sufficient to alter behavioral performance.

In AIR mice, chemogenetic inhibition of DLS-dSPNs did not affect the behavioral performance measured as number of lever presses (Fig. 4C), frequency of lever presses (Fig. 4D), head entries (Fig. 4E) and reinforcers earned (Fig. 4F). These results indicate that the function of DLS dSPNs was not necessary to sustain action execution in AIR mice.

In CIE mice, chemogenetic inhibition of DLS-dSPNs significantly reduced the total number of lever presses (Fig. 4G), the lever pressing frequency (Fig. 4H) and the number of reinforcers earned (Fig. 4J), whereas the number of head entries remained unchanged (Fig. 4I). This analysis indicated that hM4D(Gi)- expressing ^{CIE}Cre+ mice showed fewer and slower lever presses and fewer rewards earned during CNO treatment than ^{CIE}Cre- mice. These results indicate that the function of DLS dSPNs becomes necessary for action execution in CIE mice. Overall, our findings indicate that strengthened DLS-SNr synapses contribute to an abnormal functional control of action execution following chronic alcohol exposure.

Discussion

Here we describe a distinctive functional organization of striatal and subthalamic synaptic inputs to the medial and lateral SNr and investigate alcohol effects on distinct SNr subcircuits. We found that chronic inhalational alcohol exposure potentiated the inputs from the dorsolateral striatum to the SNr, likely contributing to a circuit shift in the control of action execution by the basal ganglia.

Differential synaptic organization of inputs to the medial and lateral SNr

Subpopulations of the SNr have been previously classified based on their source of striatal input, output connectivity, and molecular identity. We found that DLS dSPNs primarily synapse onto parvalbumin-expressing (PV^+) SNr neurons, whereas the DMS dSPNs primarily innervate non-parvalbumin-expressing (PV^-) SNr neurons. Previous studies indicate that the second largest subpopulation of SNr neurons consists of $GAD2^+/VGAT^+/PV^-$ neurons[13] or $GAD2^+$ neurons[37], and future studies will address whether DMS-targeted SNr neurons fall within this category. Our results agree with an enrichment of PV^+ neurons in the ventrolateral SNr[34,37] and with higher R_{in} and lower baseline firing rate in PV^- over PV^+ SNr neurons[34]. Furthermore, our findings support a gradient of intrinsic neuronal properties along the medio-lateral axis of the SNr[13].
Within the SNr, PV^+ and PV^- subpopulations have been found to control distinct aspects of motor performance[23] and sleep states[37]. Therefore, the DMS and DLS inputs have the potential to control distinct SNr-dependent behavioral outputs by targeting molecularly distinct SNr neurons.

We observed specialized synaptic properties of parallel striatal inputs to the SNr, namely short-term facilitation at DLS-SNr synapses and short-term depression at DMS-SNr synapses. Previous reports using electrical or optogenetic stimulation found that short-term facilitation is characteristic of striato-nigral synapses[38,39]. These distinct synaptic properties may emerge in response to distinct functional demands of postsynaptic SNr neurons and may result from the distinct gene expression profiles of dSPNs located in the DMS and DLS, especially in those genes related to synaptic function[40]. These subcircuit-specific properties may generalize to other striatonigral projections, including the one from the ventrolateral striatum (VLS)[12,16].

Synaptic facilitation may be required at DLS-SNr synapses to sustain postsynaptic responses in SNr neurons with lower excitability. In contrast, synaptic depression at DMS-SNr synapses may contribute to faster responses in the highly excitable DMS-targeted SNr neurons. Here, we find that DMS- and DLS-targeted subpopulations of SNr neurons differ in their rebound firing capability, with a higher number of DMS-targeted neurons displaying prolonged rebound responses. We demonstrate that striatal inputs can elicit rebound responses in the majority of DMS-targeted and a subpopulation of DLS-targeted SNr neurons. Overall, we propose that the interplay between specialized synaptic input properties and neuronal intrinsic properties contributes to fine-tune signal processing in parallel SNr subcircuits[13,21].

We find that STN synaptic inputs are stronger in the lateral compared to medial SNr and scale with the R_{in} of SNr neurons. This organization allowed STN inputs to sustain firing responses throughout SNr subregions. Yet, a postsynaptic scaling of glutamatergic synapses alone was not sufficient to explain our findings, as we observed higher presynaptic release probability on STN inputs to the lateral over the medial SNr. These

different presynaptic properties may be explained as a function of molecular differences in STN subpopulations targeting the medial and lateral SNr[41], or result from distinct presynaptic modulation of these inputs.

Our findings indicate a subcircuit-specific synaptic organization in the SNr that might generalize to other synaptic inputs, including the pallidonigral projection. We speculate that a consequence of this differential organization might be a differential vulnerability of distinct synaptic inputs to the SNr in pathological conditions affecting basal ganglia functioning, including Alcohol Use Disorder and Parkinson's Disease[26,42,43].

Potentiated DLS-SNr inputs are accompanied by altered basal ganglia control of action execution following chronic alcohol exposure

Our study indicates a selective alteration of DLS-SNr but not DMS-SNr inputs following chronic alcohol exposure. In light of previous literature indicating alcohol-induced increased excitability and in vivo calcium activity of DMS dSPNs, and altered thalamic and cortical inputs to DMS dSPNs [30,31,44–46], we can't exclude that different alcohol exposure paradigms might also induce DMS-SNr synaptic input alterations. We found that chronic alcohol exposure significantly increased the PPR at DLS-SNr inputs, indicating decreased presynaptic probability of GABA release following chronic alcohol exposure. Moreover, we found increased frequency and amplitude of asynchronous IPSCs at DLS-SNr synapses indicating an increased strength of DLS-SNr inputs. Our findings imply the presence of a postsynaptic mechanism which potentiates DLS-SNr inputs via an increased number of GABAergic synapses, an increased availability of $GABA_A$ receptors, or changes in channel conductance due to modifications in their subunit composition[3,4]. In parallel, compensatory presynaptic changes might explain the increase in PPR at DLS-SNr inputs, including altered GPCR signaling.

The changes that we observed at DLS-SNr inputs may be linked to previous evidence supporting alcohol-induced DLS disinhibition. These include decreased GABAergic synaptic transmission onto SPNs in DLS in a mouse model of binge drinking[47]. Similarly, chronic alcohol drinking was found to reduce GABAergic synaptic inputs, potentiate glutamatergic inputs, and increase the excitability of SPNs in the putamen of macaque monkeys[48,49]. We previously reported that chronic intermittent ethanol vapor exposure promotes dendritic arborization of DLS SPNs and disinhibition of cortico-striatal inputs via reduced endocannabinoid-dependent plasticity[50]. These changes were found to increase the function of DLS neurons in the performance of an in vivo visual discrimination task[50]. In mice, potentiated anterior insular cortex inputs to the DLS via impaired μ-opioid dependent long-term depression[51] were implicated in maintaining alcohol binge drinking in male mice[52]. These synaptic changes may drive cellular adaptations in DLS dSPNs affecting their efferent projections to the SNr.

Here, we find that potentiated DLS-SNr but unaltered STN-SNr inputs might contribute to enhance the striatal GABAergic drive on lateral SNr neuron output in vivo. In our experiments, the impaired action execution induced by chemogenetic inhibition of DLS dSPNs in CIE mice cannot simply be explained as a generalized reduction in motor output or emerge from decreased motivation for reward retrieval, since this manipulation did not alter the number of head entries. In random ratio training, DLS dSPNs were found to progressively disengage throughout training in healthy mice[53], whereas our behavioral findings indicate that in CIE mice DLS dSPNs fail to disengage becoming necessary to sustain action execution particularly during late training sessions. These findings may have implications for behavioral flexibility in AUD, as an abnormal engagement of the sensorimotor BG circuit during action learning and execution might interfere with associative circuits in the acquisition of novel goal-directed actions.

Overall, our findings indicate that ^{L}SNr neurons differ from those in ^{M}SNr, receive differential GABAergic and GLUergic input compared to ^{M}SNr neurons, and are selectively affected by chronic ethanol exposure. The effect of chronic ethanol on lateral striatonigral inputs likely contributes to altered execution of instrumental actions.

Materials and methods

Ethical approval

Experiments were conducted in accordance with the National Institutes of Health's Guidelines for Animal Care and Use, and all experimental procedures were approved by the National Institute on Alcohol Abuse and Alcoholism Animal Care and Use Committee (protocol # LIN-DL-1). Mice were housed in groups of 2-4 in the NIAAA vivarium on a 12-hour light cycle with ad libitum access to food and water.

Animals

VGluT2-IRES-Cre mice (B6J.129S6(FVB)- Slc17a6tm2(cre)Lowl/MwarJ, Cat. No. JAX 028863), PV-IRES-Cre mice (B6.129P2-Pvalbtm1(cre)Arbr/J, Cat. No. JAX 017320), Td-Tomato mice (B6-Cg-Gt(ROSA)26Sortm14(CAGtdTomato)Hze/, Cat. No. 007914) and C57BL-6J mice were purchased from the Jackson laboratory (JAX; Bar Harbor, ME, USA). Heterozygous Drd1-Cre (STOCK Tg(Drd1-cre)FK150Gsat/Mmucd) mice were purchased from Gensat and crossed with C57BL-6J mice. VGluT2-IRES Cre and PV-IRES-Cre homozygous and heterozygous (het) male or female mice were crossed with C57BL-6J. Homozygous PV-IRES-Cre mice were crossed with homozygous Td-Tomato mice to generate PVCre-TdTom mice. Experiments were conducted on male and female mice aged >3 months. All mice involved in the CIE experiments initiated the CIE exposure between 3 and 4 months of age. Hence, mice were tested for behavior or slice electrophysiology between 4 and 5 months of age. Genotyping was performed by polymerase chain reaction (PCR) on genomic DNA from ear biopsies.

Surgical procedures

Deep anesthesia was performed in an induction chamber using 5% Isoflurane. Animals were quickly transferred to a stereotaxic frame that delivered isoflurane at 1-3% through the mouthpiece for the whole duration of the surgery. A Hamilton syringe pre-loaded with the viral solution was inserted in the brain parenchyma to target the DLS (AP: +0.9; ML: ±2.4; DV: -3.2), DMS (AP: +0.9; ML: ±1.4; DV: -3.2) or STN (AP: -1.9; ML: ±1.7; DV: -4.5). 200 nL of pAAV5-Syn-Chronos-GFP (Addgene, plasmid #59170, 5×10^{12} vg/mL) were injected in the DMS or DLS (injection rate 25 nl/ min) of C57BL-6J mice. 300 nL of AAV5-hSyn-FLEX-Chronos-GFP (UNC viral core, 7×10^{12} vg/mL) were injected in the STN (injection rate 50 nL/ min) of VGlut2-IRES-Cre mice. 300 nL of AAV2-hSyn-DIO-HM4D(Gi)-mCherry (Addgene, plasmid #50475, 7×10^{12} vg/mL) were injected in the DLS of Drd1-Cre+ mice and their Cre- littermates. For validation of DREADD effects on DS-SNr synapses, 400 nL of pAAV5-Syn-Chronos-GFP and AAV2-hSyn-DIO-HM4D(Gi)-mCherry were co-injected in the striatum of Drd1-Cre+ mice (AP: 0.9; ML: ±2; DV: -3.2). Following the injection of the viral solution, the syringe was kept in place for 5 minutes and then retracted. The wounded skin was closed using skin glue (Vetbond, 3M). Post-operative care included the administration of ketoprofen (5mg/ kg, s.c.) following surgeries and two days of recovery, where half of the cage was placed on a heated pad.

Brain slice preparation for patch-clamp experiments and validation of viral expression

Mice were deeply anesthetized with isoflurane and decapitated. The brain was collected and transferred to a slicing chamber filled with ice-cold sucrose-based cutting solution containing the following (in mM): 194 sucrose, 30 NaCl, 4.5 KCl, 26 $NaHCO_3$, 1.2 NaH_2PO_4, 10 D-glucose, 1 $MgCl_2$, saturated with 95% O_2/5% CO_2. Coronal sections (250 µm) containing the SNr, STN, or striatum were obtained using a Leica VT1200S Vibratome (Leica Microsystems, Buffalo Grove, IL) and transferred to an incubation chamber filled with artificial cerebrospinal fluid (aCSF) containing (in mM): 124 NaCl, 4.5 KCl, 26 $NaHCO_3$, 1.2 NaH_2PO_4, 10 D-glucose, 1 $MgCl_2$, and 2 $CaCl_2$, saturated with 95% O_2/5% CO_2). Slices were incubated for 45-60 minutes at 32°C and then maintained at room temperature. Slices containing the STN, SNr, or striatum were transferred to an aCSF-filled petri dish, and low-magnification epifluorescence images were acquired using a Zeiss Axiozoom microscope (Carl Zeiss, Oberkochen, Germany) via a Zeiss Axiocam MR monochrome CCD camera for validation of viral expression.

Whole-cell patch-clamp recordings and analysis

Hemislices were transferred to a recording chamber perfused with aCSF at 30–32 °C. Neurons were visualized with an upright microscope (Model BX51WI, Olympus, Waltham, MA) using a 10x air objective or 40x water objective (LUMPlanFL, 0.80 NA) and connected to a CCD camera (SciCam Pro, Scientifica) controlled via the Ocular Imaging acquisition software (Teledyne Photometrics, Tucson, Arizona). Images were obtained using the 10x objective to track the approximate location of the recorded neurons. Recordings from SNr neurons were obtained using micropipettes (2–4 MΩ) made from 1.5 mm OD/1.12 mm ID borosilicate glass with a filament (World Precision Instruments, Sarasota, FL) pulled with a P-97 puller (Sutter Instruments, Novato, CA). The intracellular solution for voltage clamp recordings of inhibitory post-synaptic currents (IPSCs) contained the following (in mM): 150 CsCl, 10 HEPES, 2.0 $MgCl_2$, 0.3 Na-GTP, 3.0 Mg-ATP, 0.2 BAPTA-4Cs, 5 QX-314. The intracellular solution for voltage clamp recordings of excitatory post-synaptic currents (EPSCs) contained the following (in mM): 114 $CsMeSO_3$, 5.0 NaCl, 1.0 TEA-Cl, 10 HEPES, 5.0 QX-314, 1.1 EGTA, 0.3 Na-GTP, 4.0 Mg-ATP. The intracellular solution for current clamp recordings contained the following (in mM): 140 mM K-Glu, 10mM HEPES, 0.1 mM $CaCl_2$, 2 mM $MgCl_2$, 1 mM EGTA, 2 mM ATP-Mg, 0.2 mM GTP-Na. Voltage clamp recordings were performed using Multiclamp 700B and a Digidata 1550B digitizer using a low-pass filter of 2 kHz and a sampling frequency of 10 kHz. Current clamp recordings were performed using Multiclamp 700B and a Digidata 1550B digitizer using a low-pass filter of

2-10 kHz and a sampling frequency of 10 kHz. Data were acquired and analyzed using pClamp 10.3 or pClamp 10.6 software (Molecular Devices, Sunnyvale, CA). To isolate IPSCs, the AMPA receptor antagonist DNQX (10 μM) and the NMDA receptor antagonist DL-AP5 (50 μM) were continuously bath applied. To isolate EPSCs, the GABAA antagonist Gabazine (10 μM) was continuously bath-applied. To record asynchronous IPSCs, a modified aCSF was used, whereby Ca^{2+} was replaced by Sr^{2+} 4mM.
SNr neurons were characterized in voltage clamp experiments (holding voltage: -50 mV) for their location, appearance, and firing frequency assessed in tight-seal (resistance >500 MΩ) cell-attached mode before the break-in, and absence of a hyperpolarization-activated current (Ih) measured using a -50 mV step in voltage-clamp mode after break-in[39]. In experiments conducted in PVCre-TdTom mice, the following procedure was followed: neurons were visualized using DIC and a tight-seal was established; next, yellow light (509-551 nm) was briefly delivered via field illumination through the microscope objective (generated via an X-Cite LED driver, Lumen dynamics, and filtered through a Cy3 filter) to label neurons as TdTom+ or TdTom-; following breakthrough, connectivity was assessed; the field of view of the slice was then changed to reduce sampling bias in the next recording attempt.
oIPSC and oEPSC amplitudes, latency to peak, PPRs, and input resistance in voltage clamp experiments (measured from the steady state of a -50 mV step) were analyzed using clampfit (pClamp suite). Input resistance in current clamp experiments (measured from the steady state of a -50 pA, 500 ms current step) was analyzed using Easy Electrophysiology (Easy Electrophysiology Ltd, London, England). Asynchronous IPSC frequency and amplitude were analyzed using Easy Electrophysiology. A minimum of 6 trials were averaged to calculate oIPSC amplitudes, PPRs, aIPSC amplitude and frequency, and input effects on SNr neuron firing. For rebound firing analysis, a baseline was defined for each cell as the average firing frequency recorded 1 second before a -50 pA, 500 ms current step, or before optogenetic stimulation of striatal inputs. Rebound responses were then analyzed by normalizing to baseline the first instantaneous frequency (fast rebound) or the average firing frequency 400 ms (prolonged rebound) following negative current injections, or 1 second following optogenetic stimulation of striatal inputs. Neurons in which firing increased by more than 5% from to baseline were defined as “rebounders.”

Optogenetic stimulation protocols for patch-clamp recordings.
The light was generated via an X-Cite LED driver (Lumen dynamics), delivered via field illumination through the microscope objective, and filtered through a single band filter to produce ~470 nm illumination. To measure absolute amplitudes of oIPSCs and oEPSCs and evoked asynchronous IPSCs, blue light pulses of 5 ms and an optical power of ~10 mW were used. To measure paired-pulse ratios, the following pulse width were used: Fig. 1B, 0.5- 2 ms; Fig. 2D, 1-5 ms; Fig. 3B, 0.5 ms; Fig. 4C, 1 ms (the optical power and pulse width were adjusted to the minimum required to produce a stable response, range 0.56 – 6 mW). For current-clamp experiments, 2-second-long trains of stimuli at 10 or 20Hz were delivered, using a pulse width of 1-5 ms and optical power of ~5 mW. For all experiments, light pulses were delivered every 20-30 seconds.

Procedure for Chronic Intermittent ethanol exposure.
Ethanol vapor exposure was conducted in Plexiglas chambers (Plas Labs Inc., Lansing, MI). A subset of chambers was used to expose mice to vaporized ethanol (CIE group), and a separate subset was used to expose mice to air (AIR group). The chambers were connected to a vaporizer. In the ethanol chamber, 95% ethanol was vaporized through air flow at a rate of 1.5-3 L/min. Vaporized ethanol was combined with another air stream to produce a total flow rate of ~10 L/ min in each chamber. A similar rate of delivery was provided in the air chamber. The rate was adjusted throughout the cycle to produce vapor ethanol concentrations of 0.160-0.240 mg/L. Vapor ethanol concentrations were assessed using a breath analyzer. Mice were exposed to 4 cycles of CIE, each consisting of 4 consecutive days in which mice were exposed to 16 hours of ethanol vapor (CIE group) or air (AIR group) followed by 8 hours of withdrawal. In between cycles, mice underwent 72h of withdrawal. Mice were not given any loading dose of ethanol or pyrazole injections before the exposure. This procedure yielded average blood ethanol levels of 165.2 ± 10.6 mg/dl. Throughout the 4 weeks of CIE exposure, mice remained in the room containing the vapor chambers. This room had the same light cycle, temperature, and humidity settings as the colony room where mice were previously housed and where mice returned following CIE.

Procedure for blood ethanol concentration measurements.
Blood was collected maximum twice from each mouse throughout the 4 weeks of CIE, with a typical interval of 2 weeks between collections. The collection was done through a caudal vein tail nick. Blood (<20 μL) was collected from the tail vein in heparinized hematocrit tubes (Fisherbrand, Cat. No. 22-362-566) and rapidly transferred for centrifugation at 10.000 rpm for 5-10 minutes. The serum was isolated, transferred to Eppendorf tubes, and diluted for further processing. Blood ethanol concentration was measured using a colorimetric assay (Pointe Scientific, MI, USA).

Operant conditioning.
48 hours following the end of the 4th CIE cycle, mice underwent food restriction to reach ~90% of their body weight. Operant training started 6-7 days following the end of the 4th CIE cycle. Mice received injections of saline or clozapine-N-oxide (CNO, 5mg/ kg) 1h before the start of each operant conditioning session. Mice were trained to lever press for 20% sucrose in operant boxes (MedAssociates). Training began with 1 day of magazine training in which no lever was presented, but sucrose was delivered at random intervals (average 60 seconds) in the magazine. All mice successfully learned to identify the magazine and consume the reward and were moved to the operant training, which started the following day. During initial training, mice were trained to lever press under a fixed ratio (FR1) schedule (1 lever press = 1 reward) for 5 days, with a time criterion of 60 minutes, after which the session was interrupted (Day 2: FR1, 5 rewards; Day 3: FR1, 15 rewards; Day 4-6: FR1, 30 rewards). Mice were then moved to a random ratio (RR) schedule in which they received a reward after an average of 10 lever presses (RR10, Day 7-8) and then after an average of 20 lever presses (RR20, Day 9-12), for a maximum of 30 rewards over 60 minutes.

Immunohistochemistry and confocal imaging.
Mice were anesthetized with pentobarbital (50 mg/ kg) before transcardial perfusion with 1x PBS, followed by 4% formaldehyde (FA) (4% paraformaldehyde in 1x PBS). Brains were kept in 4% FA overnight and then transferred to 1x PBS until slicing. Free-floating sections (50 µm) were cut using a Pelco easySlicer Vibratome (Ted Pella Inc., Redding, CA, USA). Slices were washed for 3 x 5 minutes in 1x PBS and then incubated in a blocking solution containing 5% normal goat serum in PBS-T (0.2% Triton X-100). Slices were then incubated over 2 nights in 1x PBS containing the primary antibody (Rabbit anti-RFP, Rockland, Cat. No 600-401-379). Slices were then washed 3 x 5 minutes in 1x PBS and incubated in 1x PBS containing the secondary antibodies for 2 hours (Alexa Fluor 594 goat anti-rabbit, Invitrogen A11012, 1:500). A final wash of 3 x 5 minutes was performed before mounting using DAPI Fluoromount-G® (Southern Biotech, Cat No. 0100-20). Low-magnification epifluorescence images were obtained through a Zeiss Axiozoom microscope (Carl Zeiss, Oberkochen, Germany) equipped with standard Cy3 filters via a Zeiss Axiocam MR monochrome CCD camera.

Viruses and Reagents.
Viruses were aliquoted in 2.5- 5 µL aliquots and stored at -80 until use. All drugs (DNQX, DL-AP5, Gabazine, CNO) were purchased from Tocris.

Statistical analysis
Statistical analysis was performed in GraphPad Prism (GraphPad Software, La Jolla, California), and data was pre-processed in Excel. A ROUT test (Q = 0.1%) was used to identify statistical outliers, and based on this criterion we excluded one neuron from the analysis in Fig. 1E. Data were analyzed using two-way RM ANOVA, mixed-effects analysis with no correction, three-way ANOVA, unpaired t-tests or Mann-Whitney tests. Post-hoc comparisons were analyzed using the Šidák post-hoc test where appropriate. The statistical test used, and the significance, are indicated in the figures and figure legends. The Shapiro-Wilk test was used to determine if data were normally distributed. Significance was set at $p < 0.05$ in all analyses and indicated in figures ($^{*,\#,\$}$ for $p < 0.05$; $^{**,\#\#,\$\$}$ for $p < 0.01$; $^{***,\#\#\#,\$\$\$}$ for $p < 0.001$; $^{****,\#\#\#\#,\$\$\$\$}$ for $p < 0.0001$). All data are reported as mean + sem. Figure schematics were created with BioRender (Scientific Image and Illustration Software | BioRender).

References

1. *Diagnostic and Statistical Manual of Mental Disorders, Fifth Edition*. (American Psychiatric Association, 2013).

2. Carvalho, A. F., Heilig, M., Perez, A., Probst, C. & Rehm, J. Alcohol use disorders. *The Lancet* **394**, 781–792 (2019).

3. Abrahao, K. P., Salinas, A. G. & Lovinger, D. M. Alcohol and the Brain: Neuronal Molecular Targets, Synapses, and Circuits. *Neuron* **96**, 1223–1238 (2017).

4. Lovinger, D. M. & Roberto, M. Synaptic Effects Induced by Alcohol. *Curr Top Behav Neurosci* (2023) doi:10.1007/7854_2022_412.

5. Egervari, G., Siciliano, C. A., Whiteley, E. L. & Ron, D. Alcohol and the brain: from genes to circuits. *Trends Neurosci* **44**, 1004–1015 (2021).

6. Yin, H. H. & Knowlton, B. J. The role of the basal ganglia in habit formation. *Nat Rev Neurosci* **7**, 464–476 (2006).

7. Dudman, J. T. & Krakauer, J. W. The basal ganglia: from motor commands to the control of vigor. *Curr Opin Neurobiol* **37**, 158–166 (2016).

8. Arber, S. & Costa, R. M. Networking brainstem and basal ganglia circuits for movement. *Nat Rev Neurosci* **23**, 342–360 (2022).

9. Grillner, S. & Robertson, B. The Basal Ganglia Over 500 Million Years. *Curr Biol* **26**, R1088–R1100 (2016).

10. Koob, G. F. & Volkow, N. D. Neurocircuitry of Addiction. *Neuropsychopharmacol* **35**, 217–238 (2010).

11. Deniau, J. M., Mailly, P., Maurice, N. & Charpier, S. The pars reticulata of the substantia nigra: a window to basal ganglia output. *Prog Brain Res* **160**, 151–172 (2007).

12. Lee, J., Wang, W. & Sabatini, B. L. Anatomically segregated basal ganglia pathways allow parallel behavioral modulation. *Nat Neurosci* **23**, 1388–1398 (2020).

13. McElvain, L. E. *et al.* Specific populations of basal ganglia output neurons target distinct brain stem areas while collateralizing throughout the diencephalon. *Neuron* **109**, 1721-1738.e4 (2021).

14. Hikosaka, O. GABAergic output of the basal ganglia. in *Progress in Brain Research* vol. 160 209–226 (Elsevier, 2007).

15. Alexander, G. E., DeLong, M. R. & Strick, P. L. Parallel organization of functionally segregated circuits linking basal ganglia and cortex. *Annu Rev Neurosci* **9**, 357–381 (1986).

16. Foster, N. N. *et al.* The mouse cortico-basal ganglia-thalamic network. *Nature* **598**, 188–194 (2021).

17. Redgrave, P. *et al.* Goal-directed and habitual control in the basal ganglia: implications for Parkinson's disease. *Nat Rev Neurosci* **11**, 760–772 (2010).

18. Hintiryan, H. *et al.* The mouse cortico-striatal projectome. *Nat Neurosci* **19**, 1100–1114 (2016).

19. Hunnicutt, B. J. *et al.* A comprehensive excitatory input map of the striatum reveals novel functional organization. *Elife* **5**, e19103 (2016).

20. Deniau, J. M., Menetrey, A. & Charpier, S. The lamellar organization of the rat substantia nigra pars reticulata: Segregated patterns of striatal afferents and relationship to the topography of corticostriatal projections. *Neuroscience* **73**, 761–781 (1996).

21. Liu, D. *et al.* A common hub for sleep and motor control in the substantia nigra. *Science* **367**, 440–445 (2020).

22. Lee, C. R. & Tepper, J. M. Morphological and physiological properties of parvalbumin- and calretinin-containing gamma-aminobutyric acidergic neurons in the substantia nigra. *J Comp Neurol* **500**, 958–972 (2007).

23. Rizzi, G. & Tan, K. R. Synergistic Nigral Output Pathways Shape Movement. *Cell Rep* **27**, 2184-2198.e4 (2019).

24. Delgado-Zabalza, L. *et al.* Targeting parvalbumin-expressing neurons in the substantia nigra pars reticulata restores motor function in parkinsonian mice. *Cell Reports* **42**, 113287 (2023).

25. Gremel, C. M. & Lovinger, D. M. Associative and sensorimotor cortico-basal ganglia circuit roles in effects of abused drugs. *Genes Brain Behav* **16**, 71–85 (2017).

26. Sitzia, G. & Lovinger, D. M. Circuit dysfunctions of associative and sensorimotor basal ganglia loops in alcohol use disorder: insights from animal models. *Addiction Neuroscience* **5**, 100056 (2023).

27. Corbit, L. H., Nie, H. & Janak, P. H. Habitual alcohol seeking: time course and the contribution of subregions of the dorsal striatum. *Biol Psychiatry* **72**, 389–395 (2012).

28. Corbit, L. H., Nie, H. & Janak, P. H. Habitual responding for alcohol depends upon both AMPA and D2 receptor signaling in the dorsolateral striatum. *Front Behav Neurosci* **8**, 301 (2014).

29. Patton, M. H., Roberts, B. M., Lovinger, D. M. & Mathur, B. N. Ethanol Disinhibits Dorsolateral Striatal Medium Spiny Neurons Through Activation of A Presynaptic Delta Opioid Receptor. *Neuropsychopharmacology* **41**, 1831–1840 (2016).

30. Ma, T. *et al.* Bidirectional and long-lasting control of alcohol-seeking behavior by corticostriatal LTP and LTD. *Nat Neurosci* **21**, 373–383 (2018).

31. Roltsch Hellard, E. *et al.* Optogenetic control of alcohol-seeking behavior via the dorsomedial striatal circuit. *Neuropharmacology* **155**, 89–97 (2019).

32. Renteria, R., Baltz, E. T. & Gremel, C. M. Chronic alcohol exposure disrupts top-down control over basal ganglia action selection to produce habits. *Nat Commun* **9**, 211 (2018).

33. Renteria, R. *et al.* Mechanism for differential recruitment of orbitostriatal transmission during actions and outcomes following chronic alcohol exposure. *Elife* **10**, e67065 (2021).

34. Delgado-Zabalza, L. *et al. Targeting Parvalbumin-Expressing Neurons in the Substantia Nigra Pars Reticulata Restores Motor Function in Parkinsonian Mice*. https://www.ssrn.com/abstract=4402123 (2023) doi:10.2139/ssrn.4402123.

35. Schmidt, R., Leventhal, D. K., Mallet, N., Chen, F. & Berke, J. D. Canceling actions involves a race between basal ganglia pathways. *Nat Neurosci* **16**, 1118–1124 (2013).

36. Labouesse, M. A. *et al.* A non-canonical striatopallidal Go pathway that supports motor control. *Nat Commun* **14**, 6712 (2023).

37. Liu, D. *et al.* A common hub for sleep and motor control in the substantia nigra. *Science* **367**, 440–445 (2020).

38. Connelly, W. M., Schulz, J. M., Lees, G. & Reynolds, J. N. J. Differential short-term plasticity at convergent inhibitory synapses to the substantia nigra pars reticulata. *J Neurosci* **30**, 14854–14861 (2010).

39. Brown, J., Pan, W.-X. & Dudman, J. T. The inhibitory microcircuit of the substantia nigra provides feedback gain control of the basal ganglia output. *eLife* **3**, e02397 (2014).

40. Roman, K. M. *et al.* Spiny projection neurons exhibit transcriptional signatures within subregions of the dorsal striatum. *Cell Rep* **42**, 113435 (2023).

41. Wallén-Mackenzie, Å. *et al.* Spatio-molecular domains identified in the mouse subthalamic nucleus and neighboring glutamatergic and GABAergic brain structures. *Commun Biol* **3**, 338 (2020).

42. Mallet, Delgado, Chazalon, Miguelez, & Baufreton. Cellular and Synaptic Dysfunctions in Parkinson's Disease: Stepping out of the Striatum. *Cells* **8**, 1005 (2019).

43. Shen, W., Zhai, S. & Surmeier, D. J. Striatal synaptic adaptations in Parkinson's disease. *Neurobiol Dis* **167**, 105686 (2022).

44. Wang, J. *et al.* Alcohol Elicits Functional and Structural Plasticity Selectively in Dopamine D1 Receptor-Expressing Neurons of the Dorsomedial Striatum. *J Neurosci* **35**, 11634–11643 (2015).

45. Cheng, Y. *et al.* Distinct Synaptic Strengthening of the Striatal Direct and Indirect Pathways Drives Alcohol Consumption. *Biol Psychiatry* **81**, 918–929 (2017).

46. Baltz, E. T., Renteria, R. & Gremel, C. M. Chronic alcohol exposure differentially alters calcium activity of striatal cell populations during actions. *Addict Neurosci* **8**, 100128 (2023).

47. Wilcox, M. V. *et al.* Repeated binge-like ethanol drinking alters ethanol drinking patterns and depresses striatal GABAergic transmission. *Neuropsychopharmacology* **39**, 579–594 (2014).

48. Cuzon Carlson, V. C. *et al.* Synaptic and morphological neuroadaptations in the putamen associated with long-term, relapsing alcohol drinking in primates. *Neuropsychopharmacology* **36**, 2513–2528 (2011).

49. Cuzon Carlson, V. C., Grant, K. A. & Lovinger, D. M. Synaptic adaptations to chronic ethanol intake in male rhesus monkey dorsal striatum depend on age of drinking onset. *Neuropharmacology* **131**, 128–142 (2018).

50. DePoy, L. *et al.* Chronic alcohol produces neuroadaptations to prime dorsal striatal learning. *Proc Natl Acad Sci U S A* **110**, 14783–14788 (2013).

51. Muñoz, B., Fritz, B. M., Yin, F. & Atwood, B. K. Alcohol exposure disrupts mu opioid receptor-mediated long-term depression at insular cortex inputs to dorsolateral striatum. *Nat Commun* **9**, 1318 (2018).

52. Haggerty, D. L. *et al.* The role of anterior insular cortex inputs to dorsolateral striatum in binge alcohol drinking. *Elife* **11**, e77411 (2022).

53. Gremel, C. M. & Costa, R. M. Orbitofrontal and striatal circuits dynamically encode the shift between goal-directed and habitual actions. *Nat Commun* **4**, 2264 (2013).

Acknowledgments
The authors thank Dr. Pamela Ilse Alonso and Dr. Jeong Lee for assistance with CIE procedures and helpful discussions, Zev Jarret, Noa Reuveni and Stephanie Ramos Maciel for support in surgical procedures and preparation of slices for validation of viral expression. The authors also thank the NIAAA animal care staff for supporting animal husbandry and veterinary care, and Dr. Guoxiang Luo for performing genotyping.

Author contributions
Conceptualizations: G.S., S.B., D.M.L.; Methodology: G.S. and S.B.; Investigation: G.S., A.G. Supervision and funding acquisition: D.M.L.; Writing-original draft: G.S.; Writing-review and editing: G.S., S.B., D.M.L.

Funding
This work was supported by the National Institutes of Health, National Institute on Alcohol Abuse and Alcoholism, Division of Intramural Clinical and Biological Research (ZIAAA000416). SB was supported by the Center on Compulsive Behaviors at NIH.

Competing interests
The authors declare they have no competing interests.

Data and materials availability
All data required to evaluate the conclusions of the paper are present in the paper and in the supplementary statistical and raw data summary.

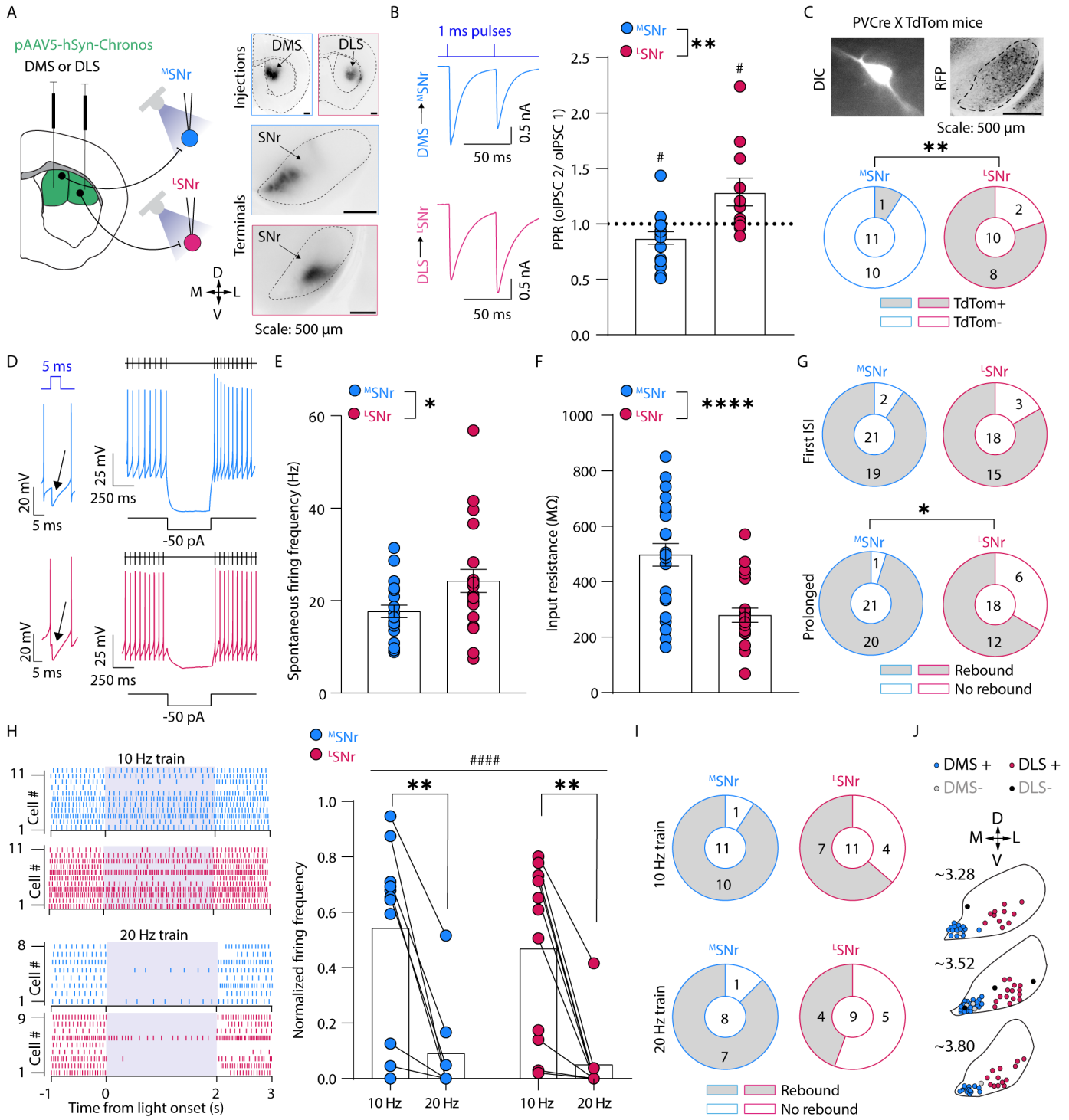

Figure 1: Input-output organization of DMS-SNr and DLS-SNr projections

A: Left: Viral injection schematic; Right: validation of Chronos-GFP expression in DMS/ DLS (injection sites, top) and SNr (terminals, bottom). **B**: Paired pulse ratio at DMS-^{M}SNr (N = 17 cells, 10 slices, 6 mice) and DLS-^{L}SNr synapses (N = 11 cells, 10 slices, 5 mice) (one sample t-test hypothetical value 1, DMS-^{M}SNr p = 0,04 and DLS-^{L}SNr p = 0.045; Mann-whitney test, two tailed, p = 0.0024). **C**: Quantification of PV expressing (TdTom^{+}) and not expressing (TdTom^{-}) neurons among DMS-targeted (N = 11 cells, 7 slices, 4 mice) and DLS-targeted SNr cells (N = 10 cells, 9 slices, 4 mice) (Fisher's exact test, p = 0.0019). **D**: Example traces and protocols for electrophysiological characterization of DMS-targeted and DLS-targeted SNr neurons. **E**: Spontaneous firing frequency of DMS-targeted (N = 21 cells, 17 slices, 7 mice) and DLS-targeted SNr neurons (N = 21 cells, 14 slices, 6 mice) (Mann-Whitney test, two-tailed, p = 0.043). **F**: Input resistance of DMS-targeted (N = 24 cells, 17 slices, 6 mice) and DLS-targeted (N = 22 cells, 15 slices, 7 mice) SNr neurons (Unpaired t-test, two-tailed, p < 0.0001). **G**: Proportion of ^{M}SNr and ^{L}SNr neurons displaying fast or prolonged (fisher's exact test, p = 0.035) rebound responses. **H:** Effects of DMS inputs (N = 11 cells, 10 Slices, 4 mice) and DLS inputs (N = 11 cells, 9 slices, 3 mice) on SNr neuron firing (mixed effects analysis, frequency main effect $F_{1, 20}$ = 25.74, p < 0.0001; Šídák's multiple comparisons test, DMS-^{M}SNr p = 0.0016, DLS-^{L}SNr p = 0.0024). **I**: Proportion of neurons displaying rebound firing following DMS-^{M}SNr and DLS-^{L}SNr input stimulation at 10 Hz or 20 Hz. **J**: Location of the DMS-targeted and DLS-targeted SNr neurons presented in Fig. 1.

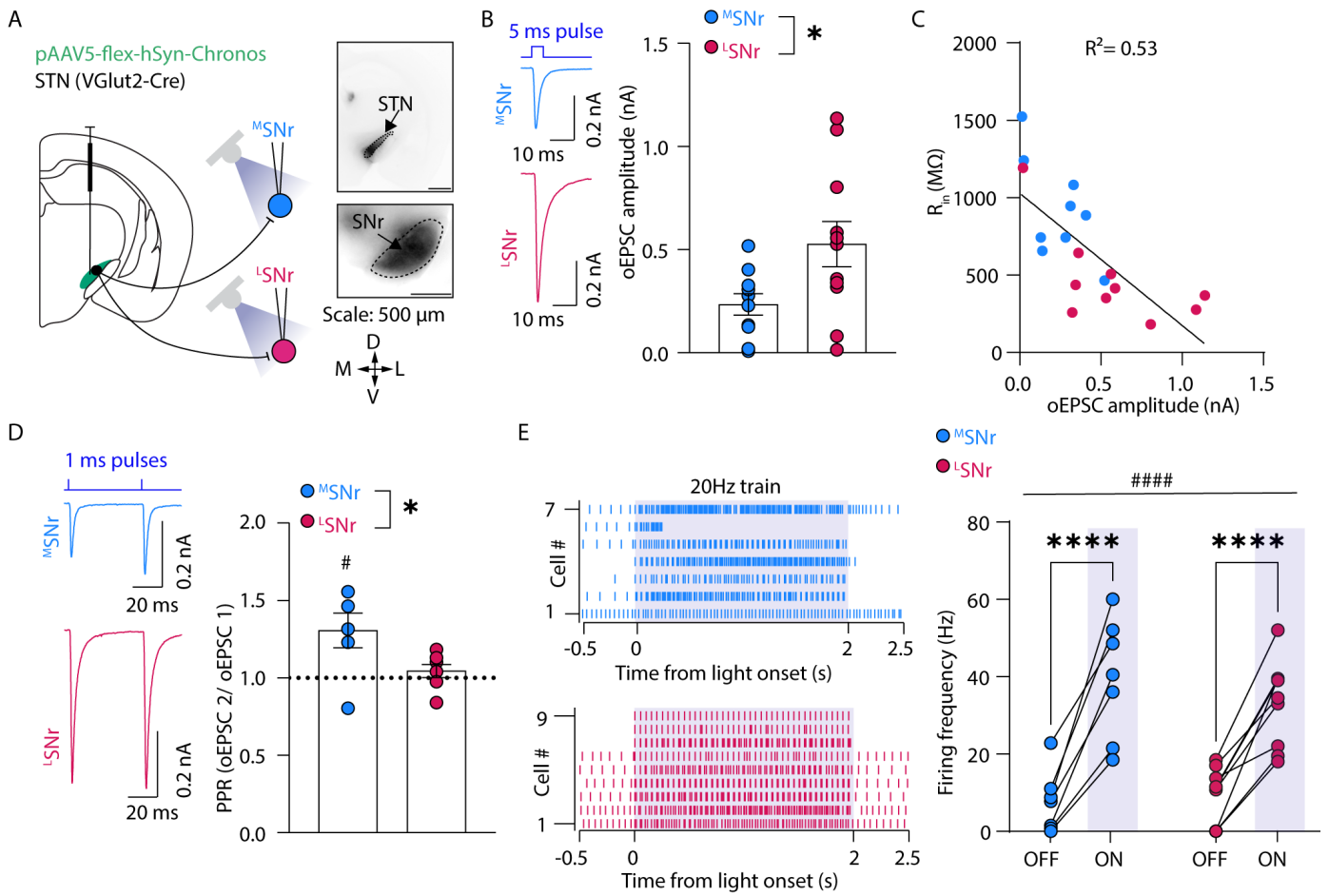

Figure 2: Differential organization of STN inputs to the medial and lateral SNr

A: Left: Viral injection schematic; Right: validation of Chronos-GFP expression in STN (injection site, top) and SNr (terminals, bottom). **B**: Amplitude of oEPSCs at STN-^{M}SNr (N = 10 cells, 10 slices, 5 mice) and STN-^{L}SNr (N = 11 cells, 10 slices, 6 mice) synapses (unpaired t-test, two-tailed, p = 0.031). **C:** Correlation of oEPSC amplitude and R_{in} at STN-SNr synapses (N = 19 cells, 14 slices, 6 mice) (R^2 = 0.53; p = 0.0004). **D**: Paired pulse ratio at STN-^{M}SNr (N = 6 cells, 6 slices, 5 mice) and STN-^{L}SNr synapses (N = 7 cells, 6 slices, 4 mice) (one sample t-test hypothetical value 1, STN-^{M}SNr p = 0.04; unpaired t-test, two-tailed, p = 0.04). **E**: Effects of STN inputs on ^{M}SNr neuron firing (N = 7 cells, 7 slices, 4 mice) and ^{L}SNr neuron firing (N = 9 cells, 8 slices, 3 mice) (2-way RM ANOVA, main effect of light $F_{1,14}$ = 109.4, p < 0.0001; Šídák's multiple comparisons test ^{M}SNr p < 0.0001; ^{L}SNr P < 0.0001).

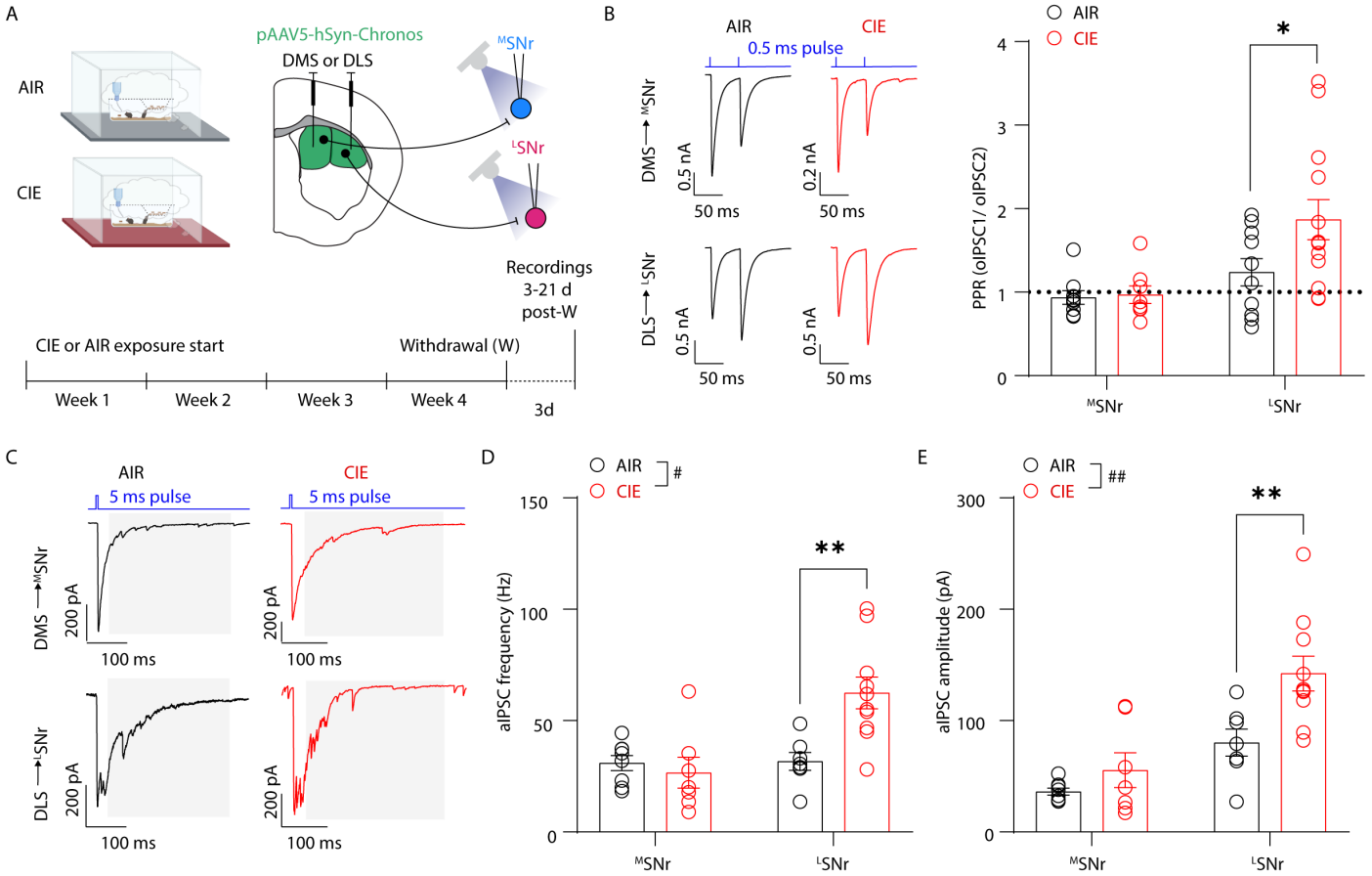

Figure 3: CIE potentiates DLS-SNr projections

A: Experimental schematic and timeline. **B**: CIE effects on paired pulse ratios at DMS-^{M}SNr (AIR: N = 9 cells, 7 slices, 4 mice; CIE: N = 7 cells, 7 slices, 5 mice) and DLS-^{L}SNr synapses (AIR: N = 11 cells, 7 slices, 4 mice; CIE: N = 13 cells, 9 slices, 5 mice) (2-way RM ANOVA, main effect of treatment $F_{1, 36} = 3.567$, $p = 0.067$; main effect of synapse, $F_{1, 36} = 8.758$, $p = 0.0054$; Šídák's multiple comparisons test ^{L}SNr AIR vs ^{L}SNr CIE $p = 0.0178$). **C**: Example traces of asynchronous IPSCs recorded at DMS-^{M}SNr and DLS-^{L}SNr synapses in AIR and CIE groups. **D**: CIE effects on aIPSC frequency at DMS-^{M}SNr (AIR: N = 8 cells, 5 slices, 3 mice; CIE: N = 7 cells, 4 slices, 3 mice) and DLS-^{L}SNr synapses (AIR: N = 7 cells, 4 slices, 3 mice; CIE: N = 10 cells, 9 slices, 5 mice) (2-way RM ANOVA, main effect of treatment, $F_{1,28} = 4.87$, $p = 0.0357$; main effect of synapse, $F_{1,28} = 9.3$, $p = 0.005$; interaction treatment x synapse, $F_{1,28} = 8.5$, $p = 0.0067$; Šídák's multiple comparisons test ^{L}SNr AIR vs ^{L}SNr CIE $p = 0.0018$). **E**: CIE effects on aIPSC amplitude (AIR: N = 8 cells, 5 slices, 3 mice; CIE: N = 7 cells, 4 slices, 3 mice) at DMS-^{M}SNr and DLS-^{L}SNr (AIR: N = 7 cells, 4 slices, 3 mice; CIE: N = 10 cells, 9 slices, 5 mice) synapses (2-way RM ANOVA, main effect of treatment, $F_{1,28} = 9.254$, $p = 0.0051$; main effect of synapse, $F_{1,28} = 23.97$, $p < 0.0001$; Šídák's multiple comparisons test ^{L}SNr AIR vs ^{L}SNr CIE $p = 0.0044$).

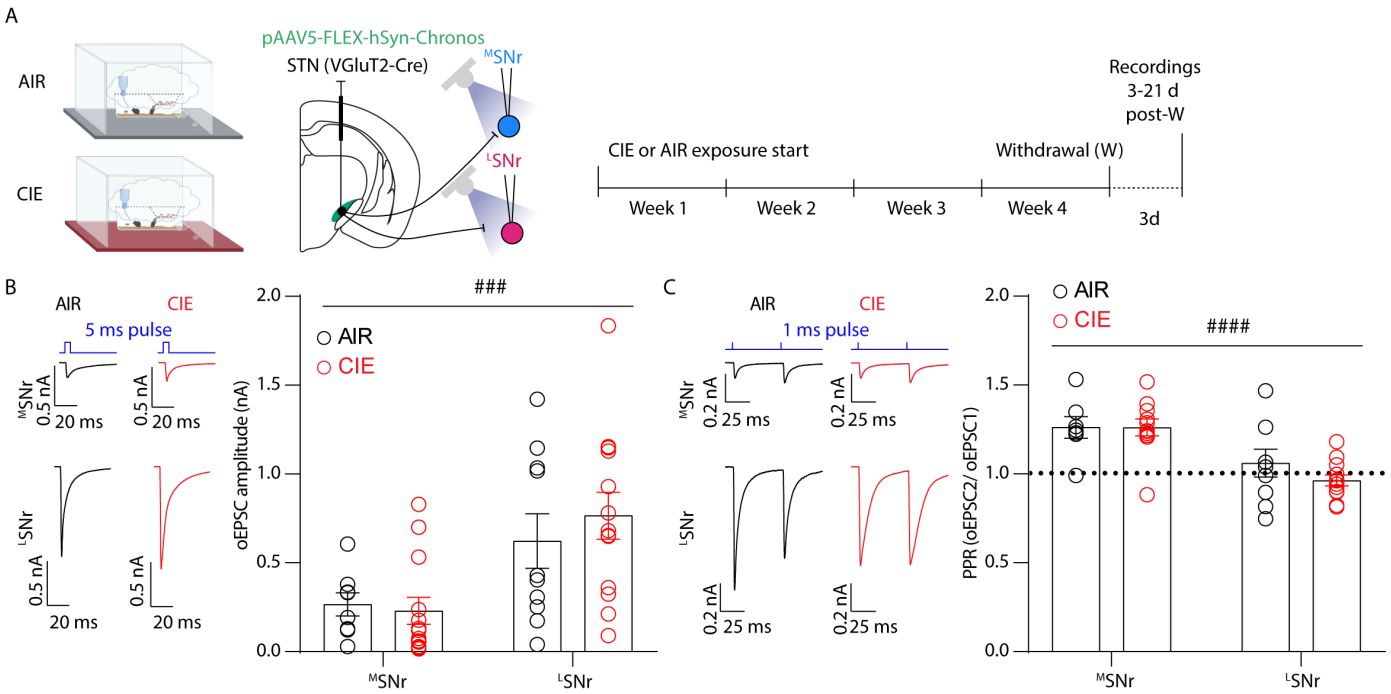

Figure 4: CIE does not affect STN-SNr inputs

A: Experimental schematic for viral injections and timeline of AIR or CIE exposure and electrophysiological recordings. **B**: CIE effects on the amplitude of oEPSCs at STN-^{M}SNr (AIR: N = 8 cells, 8 slices, 3 mice; CIE: N = 13 cells, 13 slices, 4 mice) and STN-^{L}SNr (AIR: N = 10 cells, 10 slices, 4 mice; CIE: N = 13 cells, 13 slices, 5 mice) synapses (2-way ANOVA, main effect of location, $F_{1, 40} = 14.01$, $p = 0.0006$). **C**: CIE effects on paired pulse ratios at STN-^{M}SNr (AIR: N = 7 cells, 7 slices, 3 mice; CIE: N = 11 cells, 11 slices, 4 mice) and STN-^{L}SNr (AIR: N = 9 cells, 9 slices, 3 mice; CIE: N = 12 cells, 12 slices, 5 mice) synapses (2-way ANOVA, main effect of location, $F_{1, 35} = 21.2$, $p < 0.0001$).

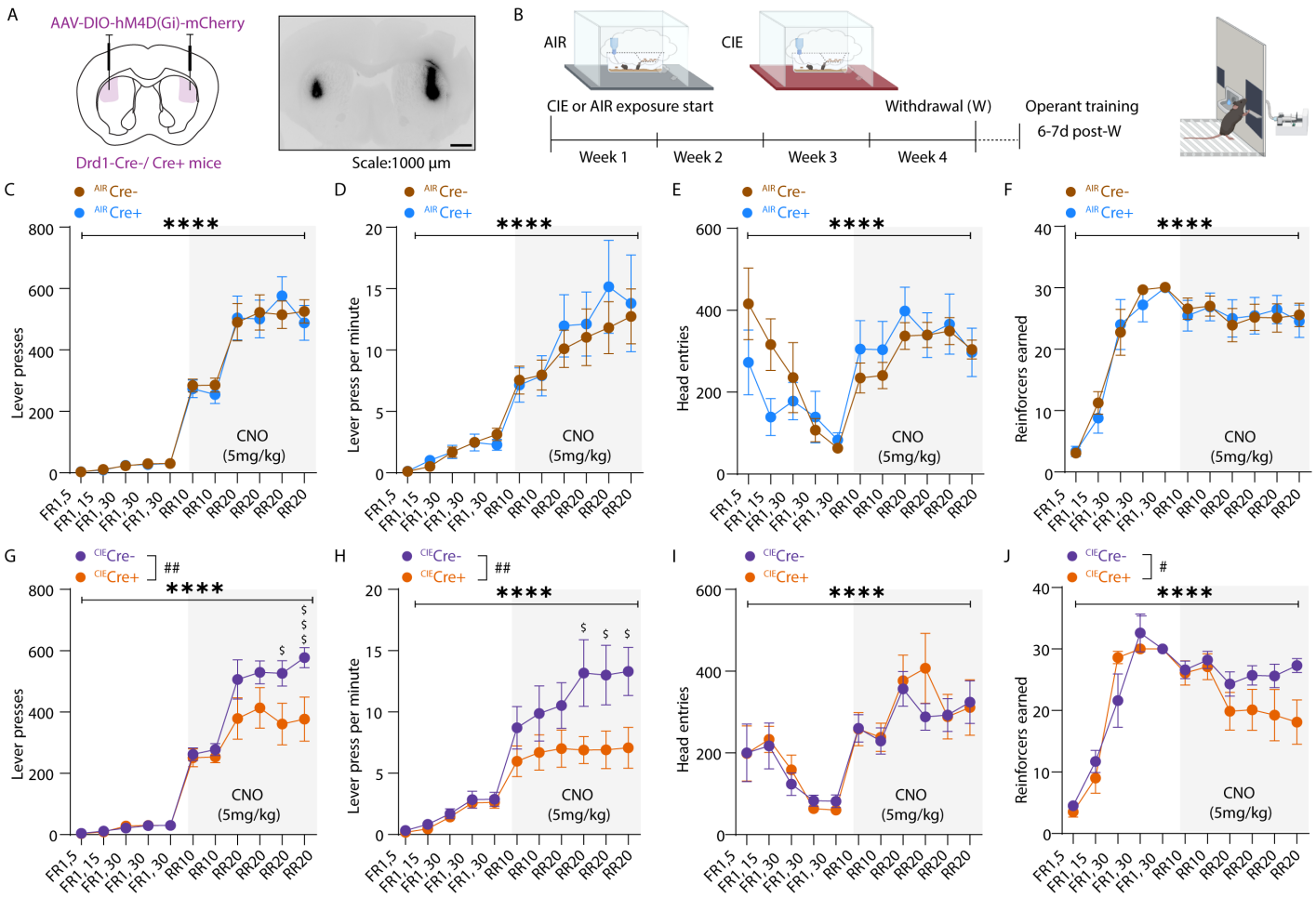

Figure 5: CIE enhances the contribution of DLS dSPNs in action execution

A: Validation of viral expression of inhibitory DREADDs in the DLS. **B**: Timeline of CIE exposure and behavioral experiments. N numbers (mice): ^{AIR}Cre- (12), ^{AIR}Cre+ (9), ^{CIE}Cre- (10), ^{CIE}Cre+ (8). **C**: Lever presses in mice (2-way RM ANOVA, main effect of session, $F_{10, 190} = 120.4$, $p < 0.0001$). **D**: Lever presses per minute in ^{AIR}Cre- and ^{AIR}Cre+ mice (2-way RM ANOVA, main effect of session, $F_{10, 190} = 28.43$, $p < 0.0001$). **E**: Head entries in ^{AIR}Cre- and ^{AIR}Cre+ mice (Mixed-effect analysis, main effect of session, $F_{10, 189} = 8.602$, $p < 0.0001$). **F**: Reinforcers earned in ^{AIR}Cre- and ^{AIR}Cre+ mice (2-way RM ANOVA, main effect of session, $F_{10, 190} = 42.76$, $p < 0.0001$). **G**: Lever presses in ^{CIE}Cre- and ^{CIE}Cre+ mice (2-way RM ANOVA, main effect of session, $F_{10, 160} = 87.82$, $p < 0.0001$; main effect of genotype, $F_{10, 16} = 4.88$, $p = 0.0421$; interaction session X genotype, $F_{10, 160} = 3.08$, $p = 0.0013$; Šídák's multiple comparisons test RR20-3 $p = 0.0122$; RR20-4 $p = 0.0009$). **H**: Lever presses per minute in ^{CIE}Cre- and ^{CIE}Cre+ mice (2-way RM ANOVA, main effect of session, $F_{10, 160} = 24.8$, $p < 0.0001$; main effect of genotype, $F_{10, 16} = 3.672$, $p = 0.0734$; interaction session X genotype, $F_{10, 160} = 2.518$, $p = 0.0077$; Šídák's multiple comparisons test RR20-2 $p = 0.0333$; RR20-3 $p = 0.0433$; RR20-4 $p = 0.0359$). **I**: Head entries in ^{CIE}Cre- and ^{CIE}Cre+ mice (2-way RM ANOVA, main effect of session, $F_{10,160} = 11.54$, $p < 0.0001$). **J**: Reinforcers earned in ^{CIE}Cre- and ^{CIE}Cre+ mice (2-way RM ANOVA, main effect of session, $F_{10, 160} = 31.54$, $p < 0.0001$; interaction session x genotype $F_{1, 16} = 2.087$, $p = 0.0283$).

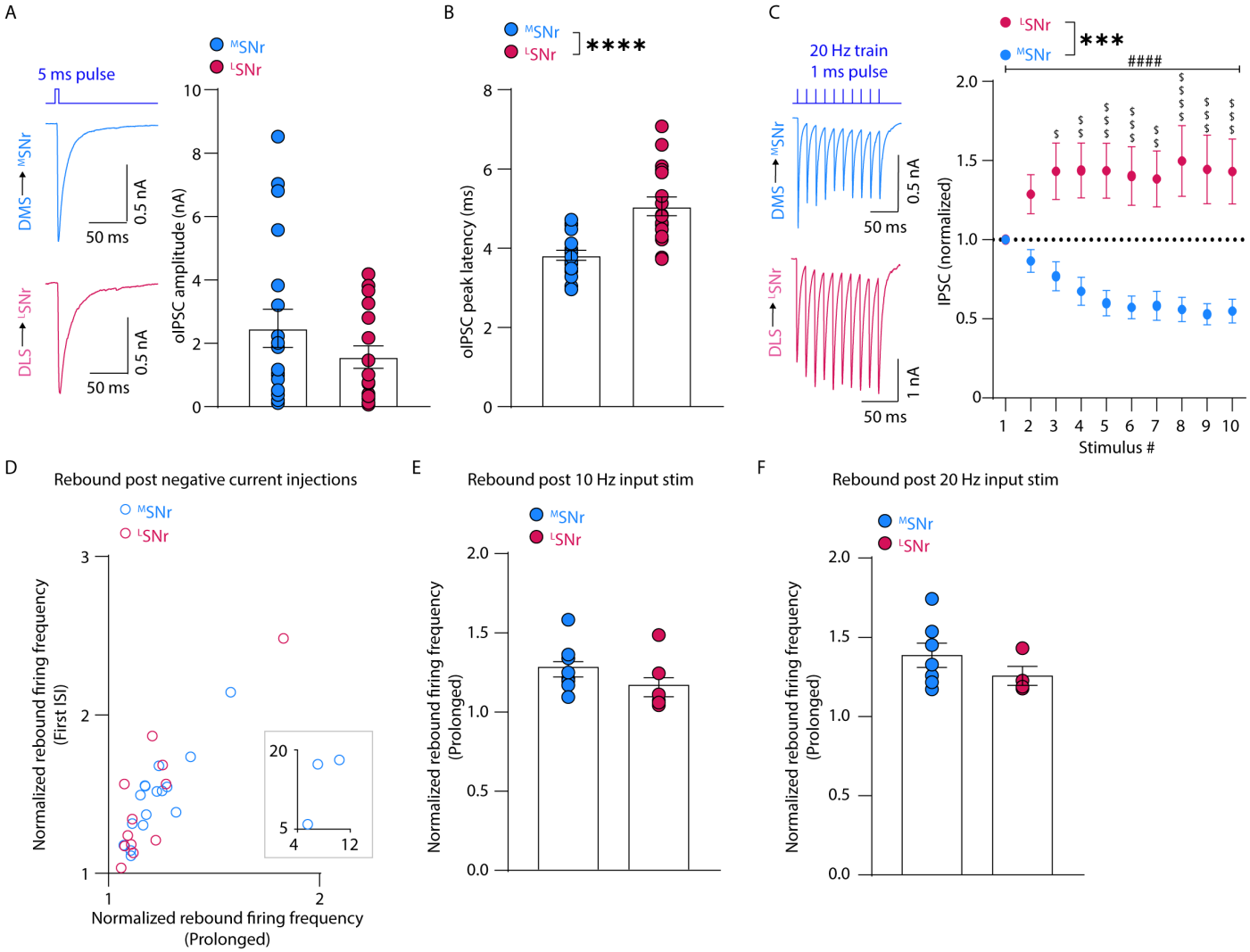

Figure supplementary 1: Synaptic characterization of DMS-SNr and DLS-SNr projections

A: Amplitude of oIPSCs at DMS-^{M}SNr (N = 19 cells, 12 slices, 6 mice) and DLS-^{L}SNr (N = 17 cells, 14 slices, 7 mice) synapses. **B**: Latency to peak of oIPSCs at DMS-^{M}SNr (N = 19 cells, 12 slices, 6 mice) and DLS-^{L}SNr (N = 17 cells, 14 slices, 7 mice) synapses (unpaired t-test, two-tailed, $p < 0.0001$). **C**: oIPSCs (normalized to 1st) during a 20 Hz train of 10 pulses at DMS-^{M}SNr (N = 10 cells, 7 slices, 5 mice) and DLS-^{L}SNr synapses (N = 11 cells, 10 slices, 5 mice) (2-way RM ANOVA, main effect of synapse, $F_{1, 19} = 14$, $p = 0.0014$; interaction synapse x pulse, $F_{9, 171} = 12.8$, $p < 0.0001$; Šídák's multiple comparisons tests). **D**: Amplitude (normalized to baseline firing rates) of fast (y axis) and prolonged (x axis) post-inhibitory rebound responses (fig. 1G) in ^{M}SNr and ^{L}SNr neurons; inset: high-rebounding ^{M}SNr neurons. **E**: Amplitude of post-inhibitory rebound responses induced by stimulating DMS or DLS inputs using a 10 Hz train. **F**: Amplitude of post-inhibitory rebound responses induced by stimulating DMS or DLS inputs using a 20 Hz train.

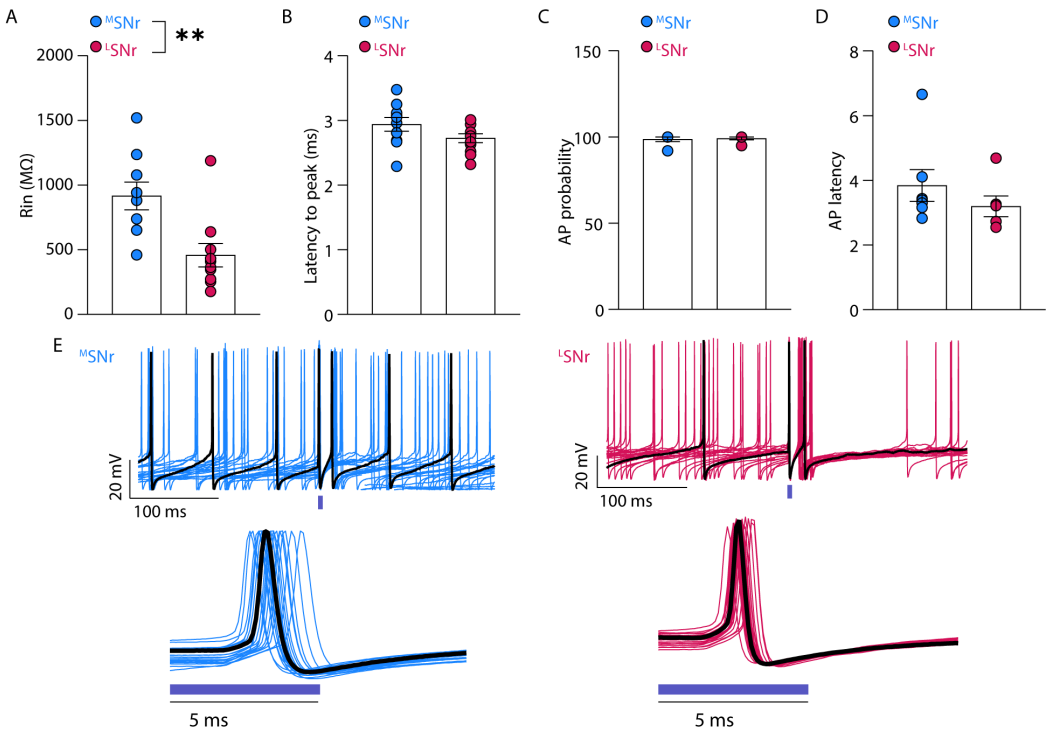

Figure supplementary 2: Functional and synaptic characterization of STN-SNr projections

A: Input resistance of ^{M}SNr (N = 9 cells, 8 slices, 5 mice) and ^{L}SNr (N = 10 cells, 10 slices, 6 mice) neurons recorded in fig. 2B-2C (Unpaired t-test, two-tailed, p = 0.0045). **B**: Latency to peak of oEPSCs recorded at STN-^{M}SNr (N = 10 cells, 10 slices, 5 mice) and STN-^{L}SNr (N = 11 cells, 10 slices, 6 mice) synapses. **C**: Probability of AP in ^{M}SNr (N = 7 cells, 6 slices, 4 mice) and ^{L}SNr (N = 6 cells, 6 slices, 3 mice) neurons upon STN input stimulation. **D**: Latency of AP in ^{M}SNr (N = 7 cells, 6 slices, 4 mice) and ^{L}SNr (N = 6 cells, 6 slices, 3 mice) neurons upon STN input stimulation. **E**: Example traces of ^{M}SNr and ^{L}SNr neuron firing during STN input stimulation.

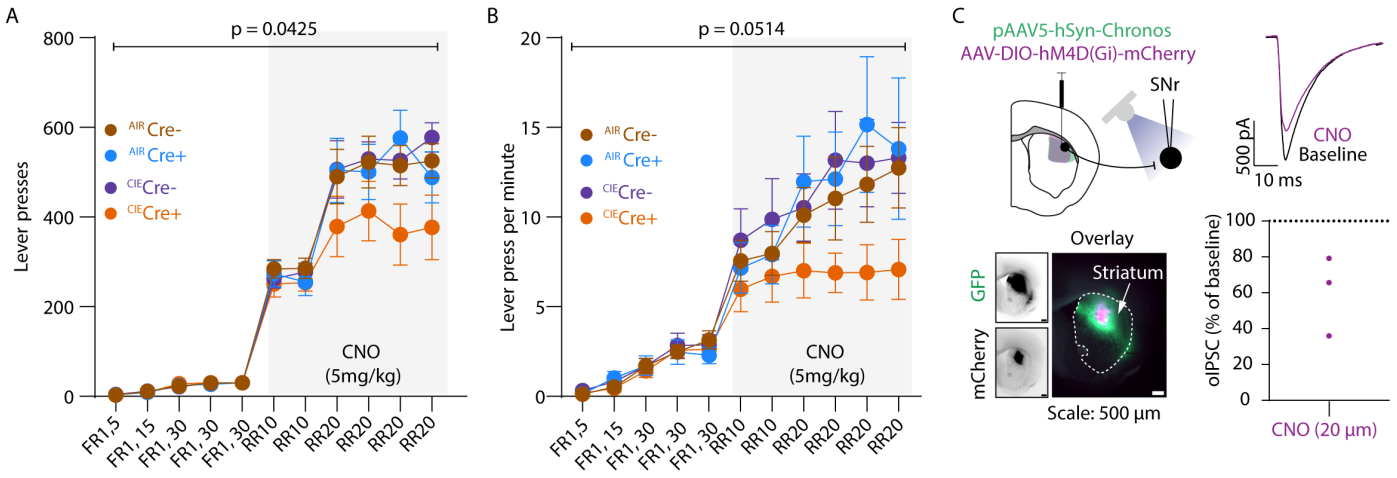

Figure supplementary 3: Behavioral and physiological effects of chemogenetic inhibition on DLS dSPN- SNr projections

A: Lever presses in ^{AIR}Cre- (N = 12), ^{AIR}Cre+ (N = 9), ^{CIE}Cre- (N = 10) and ^{CIE}Cre+ (N = 8) mice (3-way ANOVA, interaction session x treatment x genotype, $F_{10, 350} = 1.912$, $p = 0.0425$). **B**: Lever presses in ^{AIR}Cre- (N = 12), ^{AIR}Cre+ (N = 9), ^{CIE}Cre- (N = 10) and ^{CIE}Cre+ (N = 8) mice (3-way ANOVA, interaction session x treatment x genotype, $F_{10, 350} = 1.849$, $p = 0.0514$). **C**: Effect of CNO bath application on oIPSCs at DS-SNr synapses (n = 3 cells, 3 slices, 2 mice).